coverage suggests the vertical eddy diffusion profile can be estimated by a continuous function.

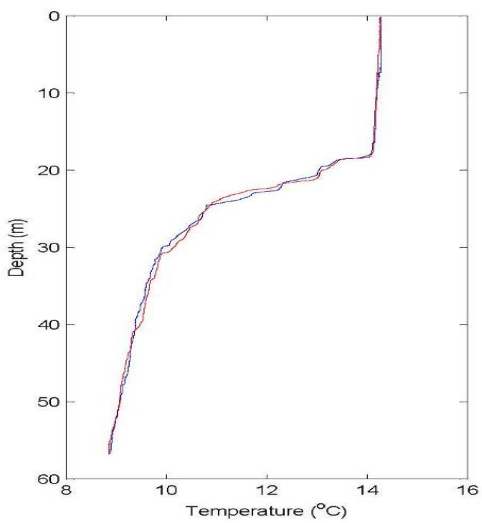

Figure 2. 16. Temperature profiles for the first (red) and last (blue) profile at the MWY location for October 30, 2003. The STL extends to about 18 meters.

Table 2. 9. STL depth averaged eddy diffusion $\langle K_e \rangle$ and energy dissipation $\langle \varepsilon \rangle$ for each profile taken on October 30, 2004 at MWY. The STL depth was about 18 meters.

Sample Time	$\langle K_e \rangle$ (m^2/s)	$\langle \varepsilon \rangle$ (m^2/s^3)
11:10	8.7×10^{-4}	6.25×10^{-8}
11:42	8.9×10^{-4}	6.25×10^{-9}
12:10	2.5×10^{-3}	2.9×10^{-8}
12:34	2.8×10^{-3}	1.9×10^{-8}

2.3.5.2 Functional Distribution for Observed Eddy Diffusion Profiles

The instantaneous eddy diffusion profiles showed turbulent mixing was patchy, but sequential profiles suggested most of the water column would experience turbulent mixing. Because the model requires eddy diffusion as a function of depth over time, a simple empirical formulation is sought based on the observed profiles. First the depth average eddy diffusion is estimated (in the STL), then a functional form was sought that characterized how eddy diffusion varied over the whole water depth.

To determine the depth-averaged K_e, each mixing patch was weighted by the patch (segment) length and the weighted terms were summed and divided by the STL depth (h_{STL}); segment weighted eddy diffusion $\langle K_e \rangle$ ranged from 2×10^{-5} m^2/s to 5×10^{-3}

m^2/s (Table 2. 10). Eddy diffusion patches varied over time with typically stronger mixing in the STL above the density interface (thermocline) and weaker mixing below the thermocline. This pattern is exemplified in the March 16 profiles (Figure 2. 14). At NWA the STL was the whole water depth and K_e was fairly uniform over the whole depth. At NOA and MWY the STL was to about 25 m and within the STL, K_e was fairly uniform but below the STL K_e was smaller. At SWA the STL was to about 12 m and within the STL K_e was uniform to about six meters and then decreased to the base of the STL; below the STL K_e was sparse and smaller than K_e in the STL. Similar patterns were observed in the other profiles (Appendix A).

Table 2. 10. STL depth-averaged eddy diffusion at NWA, NOA, MWY, and SWA for year 2004. The segment-weighted values were determined over the STL (h_{STL}), which was determined from particle and fluorescence distributions.

Date (JD)	NWA		NOA		MWY		SWA	
	$\langle K_e \rangle$ (m^2/s)	h_{STL} (m)	$\langle K_e \rangle$ (m^2/s)	h_{STL} (m)	$\langle K_e \rangle$ (m^2/s)	h_{STL} (m)	$\langle K_e \rangle$ (m^2/s)	h_{STL} (m)
3/2/04 (61.5)	0.003	34	0.0005	42	0.0002	28	0.0005	10
3/9/04 (68.5)	0.0002	34	0.0005	42	0.0002	35	0.0007	10
3/16/04 (75.5)	0.002	34	0.001	25	0.002	25	0.001	12
3/23/04 (82.5)	0.002	30	0.002	34	NA		NA	
3/30/04 (89.5)	NA		0.004	25	0.004	22	0.002	20
4/6/04 (96.5)	0.0002	8	$6x10^{-5}$	6	$2x10^{-5}$	8	0.0001	10
4/9/04 (99.5)	0.0003	10	0.0002	13	0.0001	13	0.0003	14
4/13/04 (103.5)	0.0004	26	0.003	26	0.0004	12	0.0001	8
4/16/04 (106.5)	0.005	21	0.0008	20	0.003	14	0.0004	13
4/20/04 (110.5)	NA		NA		0.002	15	0.0005	13

A general Ke profile was determined by combining all observations by location and fitting a general profile to the data (Figure 2. 17). On average, eddy diffusion was largest at the surface and smallest at some interior depth, where it increased to the bottom. At NOA, the surface was 3.4 times greater than at the bottom, at MWY it was 3.3 times greater at the surface, and at SWA it was 10 times greater (Table 2. 11). The depth where eddy diffusion starts to increase towards the bottom is deepest at NOA and shallowest at SWA (Figure 2. 17), which agrees with the observation of the persistent upward isotherm tilt from north to south. Based on the combined observations, eddy diffusion decreases from the surface to the bottom of the STL, where it can decrease further below the STL over some depth and then remains uniform to the bottom (2.27).

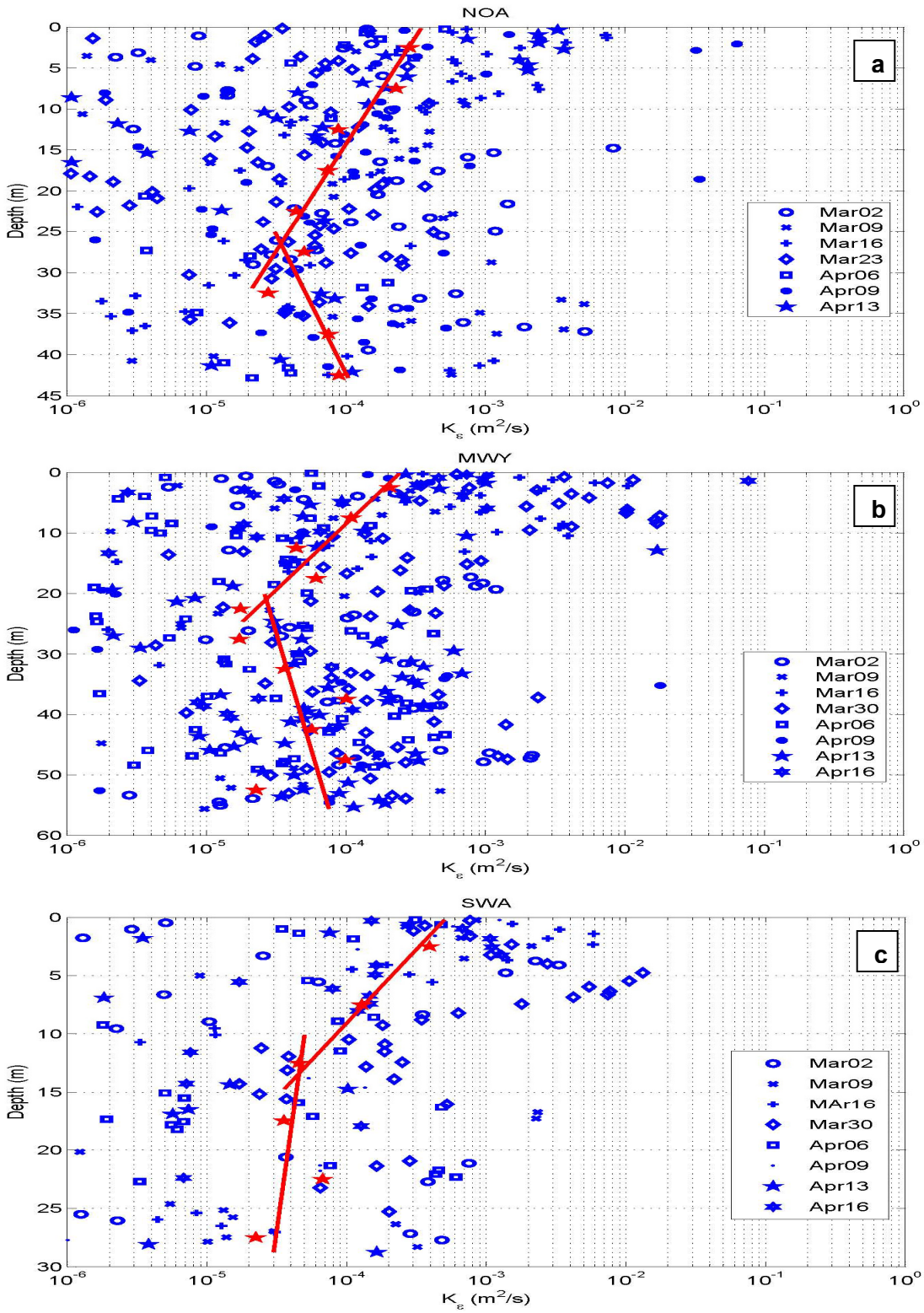

Figure 2. 17. Combined eddy diffusion observations at NOA (a), MWY (b), and SWA (c) for 2004 sample dates noted in legend. The red stars are the geometric average over a five-meter interval (star centered on the interval). The red lines were linearly interpolated lines between the red stars (Table 2. 11).

$$K(z) = \langle K_e \rangle \exp\left(\frac{z\ln(\varphi)}{h_{STL}}\right) \quad 0 \le z \le h_{STL}$$

$$K(z) = \varphi\psi \langle K_e \rangle \quad h_{STL} < z \le h_{\psi} \tag{2.27}$$

$$K(z) = \phi \langle K_e \rangle \quad h_{\psi} < z$$

Where K(z) is the depth-varying eddy diffusion, $\langle K_e \rangle$ is from Table 2. 10, z is depth, h_{STL} is depth of the STL, and φ, ψ, and ϕ are calibration coefficients that determine the functional form of K(z).

The STL depth is approximated by equation (1.17) presented in Section One and is reproduced here (2.28).

$$h_{STL} = h_1 + \frac{0.27h_1}{W_N}\left(\frac{2L_{loc}}{L}\right) \tag{2.28}$$

Where L is the lake length (31 km), h_1 is depth to the density interface, W_N is the Wedderburn Number, and L_{loc} is the station distance from the center of the lake.

Table 2. 11. Eddy diffusion values obtained from the linearly interpolated lines presented in Figure 2. 17. Values were obtained at the surface, intercept, and bottom. Lines were interpolated to the geometrically averaged points (Figure 2. 17) over the ranges specified; lower interpolation ranges were the depths below the upper ranges.

Location	K_e(surface) (m^2/s)	K_e(bottom) (m^2/s)	K_e(intercept) (m^2/s)	Upper Interpolation Depth Range (m)
NOA	3.5×10^{-4}	1.0×10^{-4}	3.4×10^{-5}	0-32
MWY	2.47×10^{-4}	7.5×10^{-5}	2.7×10^{-5}	0-25
SWA	5.2×10^{-4}	2.9×10^{-5}	4.8×10^{-5}	0-15

2.3.5.3 Observed Peclet Numbers

In Section One it was shown that the persistent isotherm tilt produced a deeper mixing depth at the north end of lake compared to the south end, and the combined eddy diffusion observations indicated deeper mixing at the north end compared to the south end; therefore, as phytoplankton travel downwind from south to north, they will be subjected to deeper mixing because of the tilt. The different mixing depths affects phytoplankton growth through the integrated photosynthesis function (2.22). How hydrodynamics affect phytoplankton growth or decay depends on the relative values of the Peclet and Growth Numbers (O'Brien et al., 2003).

The computed Peclet Numbers suggest phytoplankton success depends on a balance between vertical mixing, sinking, and growth. Pe (2.29) was generally less than ten for the individual segments and less than one for the mean Pe (2.30) (Figure 2. 18); the mean lies in the lower part of regime C and D (Figure 2. 4). In this regime, eddy diffusion and sinking velocity have an effect on phytoplankton success, which suggests that phytoplankton dynamics are governed by a balance between mixing, sinking, and growth (Huisman and Oostveen, 1999; Huisman et al., 2002). O'Brien et al. (2003) results are restricted to a well-defined mixed layer and that the particle flux at the base of the mixed layer is zero. Huisman et al. (2002) has shown that phytoplankton blooms can develop independent of water depth when the proper balance between eddy diffusion, sinking, and growth are achieved. The computed Peclet Numbers suggest the 2004 phytoplankton bloom may result from a relaxation in vertical mixing or eddy diffusion.

$$P_e = \frac{w_s l_e}{K_e} \tag{2.29}$$

$$\overline{P}_e = \exp\left(\sum \frac{l_e}{\sum l_e} \ln P_e \right) \tag{2.30}$$

Where l_e is the segment length for the observed K_e segment and w_s is 0.86 (m/d).

A note on the calculation of the Peclet number: the Peclet number could be estimated with the velocity scale of the eddy ($P_e = w_s / u_{eddy}$), where u_{eddy} scales as $u_{eddy} \approx K_e / L_c$, with L_c being the length-centered scale. Typically L_c is less than the segment length (Figure 2. 13), which means the estimated Pe in Figure 2. 18 could be smaller by a factor of 0.3 to 0.1. Such an analysis would mean that phytoplankton success is less dependent on the sinking velocity within a turbulent patch defined by L_c; u_{turb} represents the overturning velocity for eddy of size L_C and transport occurs over length L_C. As presented earlier, turbulent mixing is an overlay of many turbulent patches that eventually cover most of the water column. When a particle is within a patch, it is turbulently mixed. When it is not covered by a patch, it sinks with velocity w_s. Integrating over time and depth smoothes out the isolated events; this paper is interested in the integrated effect which occurs over larger time and space scales. For this type of transport, the appropriate measure is given by (2.29).

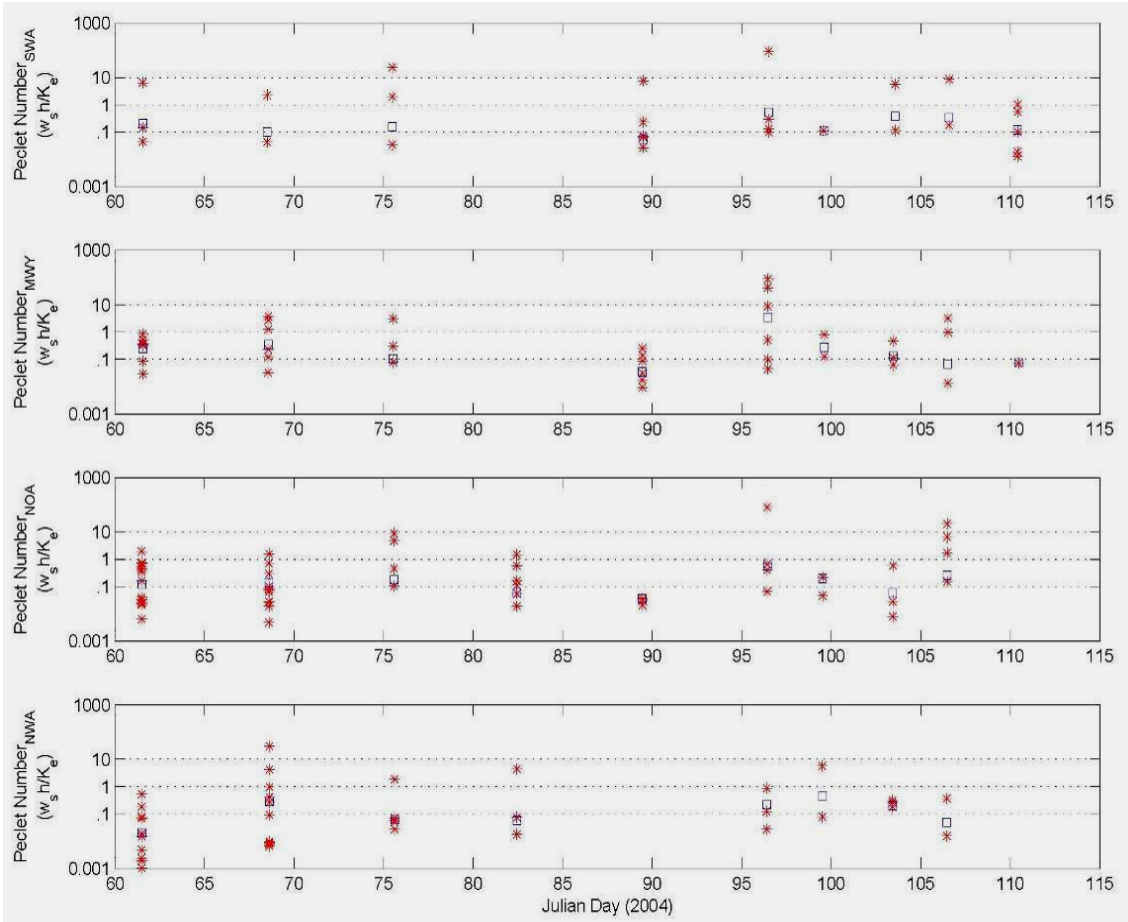

Figure 2. 18. Peclet Numbers calculated for each segment within the STL and assuming a sinking velocity (w_s) of 0.86 (m/s). Red asterisks represent each segment ($P_e=w_s l_e/K_e$, where l_e is the segment length) and blue squares represent the geometric mean of group.

2.3.6 Convective Mixing

The eddy diffusion obtained from the SCAMP profiles were obtained during the day when convective was insignificant; convective mixing can cause significant vertical mixing and typically occurs when air temperature cools over night (Brainerd and Gregg, 1993, 1993a). Eddy structure and convective mixing effects were investigated with the length-centered displacement scale (L_c) and a heat balance algorithm. Shear-induced eddies typically have scales much less than the mixed layer depth while convection typically scales over the whole mixed layer depth (Imberger and Ivey, 1991); Langmuir cells would scale with the mixed layer depth. Inspection of L_c and temperature profiles indicated vertical convection or Langmuir cells were absent or insignificant during the daytime observations (Appendix A); however, surface heat fluxes indicated surface heat loss occurred during the night

when profiles were not taken (Figure 2. 19). Heat loss at the water surface cools the surface water, which then sinks to a depth of equivalent temperature or reaches the thermocline where a small amount of water is entrained into the surface turbulent layer. This process cools the upper water and erodes the thermocline. For each SCAMP temperature profile, potential convective mixing depths were estimated for the following night based on heat loss during the night. To determine the potential convective mixing depth, a mixing algorithm was used that vertically mixed water near the surface until the net change in water temperature equaled the heat loss; temperature and heat were related by (2.31) (Thomann and Mueller, 1987).

$$\frac{\partial T}{\partial t} = \frac{\Delta H}{\rho c_p D} \tag{2.31}$$

Where T is water temperature, D is water depth, ρ is water density, c_p is specific heat content, and ΔH is the heating rate.

The change in heat is governed by surface energy fluxes for momentum, sensible heat, and latent heat that were estimated with standard bulk aerodynamic formulas, $\tau = \rho_A C_D U_Z^2$, $H = \rho_A C_A C_H U_z (T_s - T_z)$, $E = \rho_A L_V C_E U_z (q_s - q_z)$, where τ is the shear stress at the air-water interface, ρ_A air density at the air-water interface, C_D is the drag coefficient, U_Z is the wind speed at height z above the water surface; H is the sensible heat transfer, C_A is the specific heat of air, C_H is the sensible heat transfer coefficient, T_s is the surface water temperature, T_z is the air temperature at height z; E is the latent heat transfer, L_V is the latent heat of vaporization, C_E is latent heat transfer coefficient, q_s is the specific humidity at saturation pressure at Ts, q_z is specific humidity of air at height z. Over daily time scales, atmospheric stability above the water can greatly affect the transfer coefficients C_D, C_H, and C_E (Imberger and Patterson, 1990). Atmospheric stability was determined using the Monin and Obukhov (1954) stability parameter z/L, where the length scale L is defined by (2.32)

.

$$L = \frac{-\rho_A u_*^3 T_V}{kg\left(\frac{H}{C_A} + 0.61\frac{T_z E}{L_V}\right)} \tag{2.32}$$

Where T_V is the virtual air temperature $\left(=T_Z\left[1+0.61q_z\right]\right)$, k is the von Karman constant, g is gravity, and u_* is the shear velocity $\left(C_D U_Z^2\right)^{1/2}$.

Because L depends on the transfer coefficients, an iterative approach was used to estimate the transfer coefficients (Hicks, 1975). The method starts with transfer coefficient values for neutral conditions and then uses a set of similarity functions (Paulson, 1970) to update the transfer coefficients based on the Monin-Obukhov length scale L; the iteration terminates when L changes less than 0.01%. Water temperature was determined by the shallowest thermistor from the MWY array and atmospheric conditions were obtained from the I-90 floating bridge and the UW atmospheric science building (Section One). Component heat fluxes are presented in Figure 2. 19 and potential convective mixing depths are summarized in Table 2. 12.

Table 2. 12. Potential convective mixing depths based on daytime temperature profiles and the following night's heat flux (the effective temperature decrease is given in parentheses in ^{o}C). At NOA on JD 89.5, the 19-meter mixing depth was driven by a large tilt in the isotherm structure, Figure 1.24.

Julian Day	NOA (m)	MWY (m)	SWA (m)
68.5	2.2 (0.17)	3.6 (0.1)	3.2 (0.12)
75.5	4 (0.02)	3.7 (0.02)	3.7 (0.02)
82.5	3 (0.06)	NA	NA
89.5	19.5 (0.06)	9.8 (0.13)	9 (0.14)
96.5	1.3 (0.1)	1 (0.12)	1 (0.15)
99.5	1.3 (0.16)	1 (0.28)	1.3 (0.17)
103.5	4 (0.16)	5 (0.13)	1.3 (0.38)
106.5	5.7 (0.01)	4 (0.15)	4 (0.15)
110.5	NA	6 (0.04)	5.3 (0.04)

2.4 Advective/Reactive Diffusion Model

In section 2.2.2, the full Advective/Reactive Diffusion equation was reduced to the one-dimensional form by removing horizontal advection terms (2.16). The one-dimensional model was applied at NOA, MWY, and SWA. Before presenting the model results, I make the case that horizontal transport scales are sufficiently long so that the diatom dynamics are governed by kinetics rather than advective fluxes.

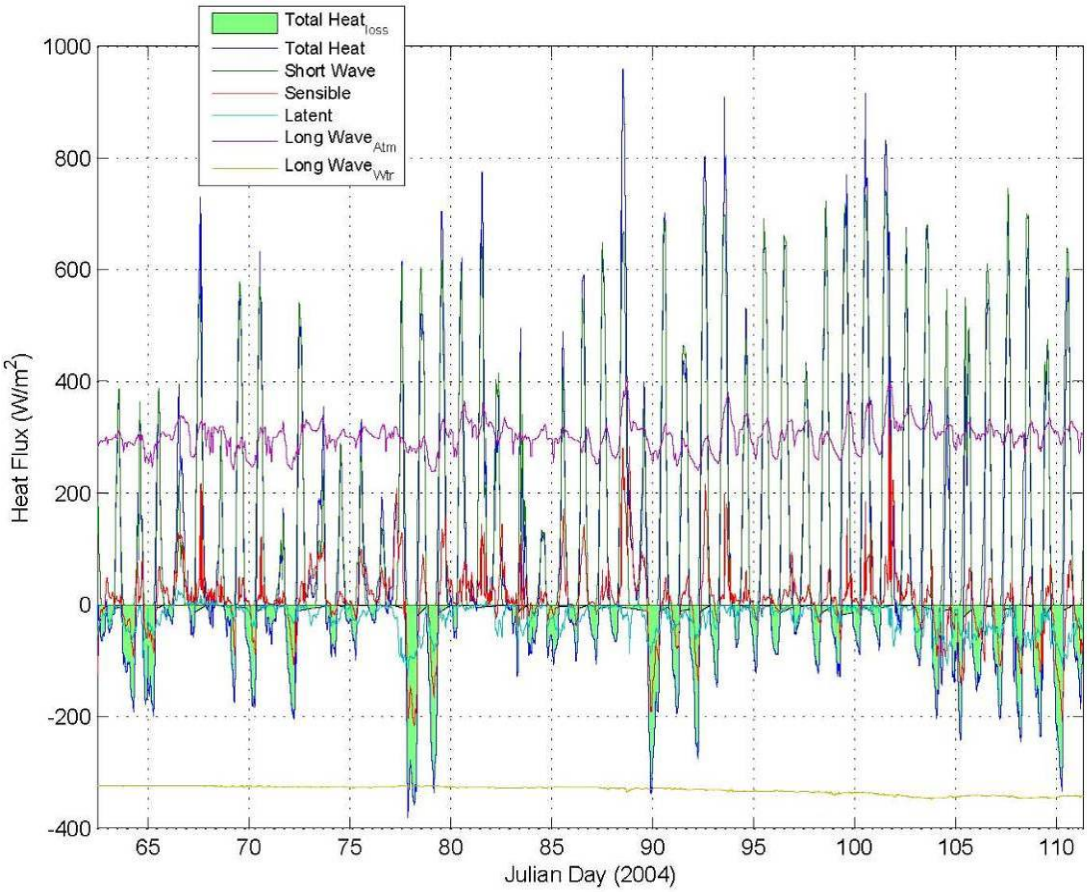

Figure 2. 19. Heat flux at the surface of Lake Washington for year 2004. Negative values indicate heat loss from the water surface (filled green).

Horizontal velocities were obtained in 2003 between JD 91 and 112. The depth and time-averaged horizontal velocity below the SR520 bridge was 1.14 cm/s from three to 11 meters and at MWY it was 0.14 cm/s from eight to 20 meters. Combining the two results gives a depth and time-averaged velocity of 0.47 cm/s from zero to 20 meters. The distance between NOA and MWY is about 9.5 km, which gives a travel between nine and 78 days (Table 2. 13). For years 2003 and 2004, in situ phytoplankton growth rates were about 0.10 and 0.07 1/day; typical in situ *A. subaractica* growth rates are around 0.07 1/day (Gibson and Foy, 1993). The average travel times are near or greater than typical e-folding growth times (Table 2. 13). This result suggests that phytoplankton could adapt to conditions between the three locations except under a vigorous wind when phytoplankton adaptation would be insignificant. If the 0.47 cm/s velocity and tilt duration of ten to 18 days are considered, only a fraction of the upwind phytoplankton population would reach the

downwind location. The 0.47 cm/s velocity is more representative of depth-averaged flow conditions between NOA and MWY. As phytoplankton are transported from NOA to MWY, the flow area increases and velocities decrease, which increases the travel time. Based on a travel time of 23 days, NOA, MWY, and SWA could be considered isolated from each other and this justifies ignoring horizontal transport in the model; however, horizontal and vertical velocities could be significant at SWA where upwelling will occur (Monismith, 1986; Farrow and Stevens, 2003).

Table 2. 13. Travel time between the MWY and NOA locations for various depth-averaged velocities. For windy events for the 2003 and 2004 periods, typical wind speeds were approximately 8 (m/s).

Velocity (cm/s)	Travel time over 9.5 km (days)	Growth time scale (days)
1.14	9	10-14
0.14	78	
.47(1)	23	
24(2)	0.46	
(1) 0-20 meter depth average of the SR520 and MWY (2) 3% of a 8 (m/s) wind		

The one-dimensional Advection/Reactive Diffusion model (2.20) was implemented to simulate phytoplankton dynamics at NOA, MWY and SWA for year 2004. The partial differential equation was approximated in finite difference form using a Crank-Nicholson semi-implicit time scheme. Eddy diffusion and temperature varied with depth and time, and phosphate, incident light, light attenuation, wind, and the STL varied with time.

2.4.1 Configuration of the Advective/Reactive Diffusion Model

The model was configured to simulate phytoplankton biovolume densities, which were approximated with the combined 5 and 16 μm particle concentrations; the simulation period was from JD 68.5 to 110.5. Initial concentrations were defined by the concentration profiles measured on JD 68.5 from which the model simulated the phytoplankton evolution to JD 110.5. Various model parameters and conditions were defined by field observations, which were discrete samples in time. Because the model was continuous in time, parameters and conditions between observations were determined by linear interpolation. Specific parameter conditions are described below. The model time step was 30 minutes and the grid spacing was one meter.

2.4.1.1 Eddy Diffusion

Measured eddy diffusion values were used in the model; however, the complicated vertical structure was approximated by (2.27) and the depth of the surface turbulent layer was approximated by (2.28) with $\langle K_e \rangle$ varying over time as described in Table 2. 10. Bottom eddy diffusion was defined as a fraction of the surface eddy diffusion (ϕ), which remained constant over time (Table 2. 14). The three parameters φ, ψ, and ϕ determine the shape of the eddy diffusion profile. These parameters were calibration coefficients and the values that produced the best simulated phytoplankton profiles (visual comparison) are given in Table 2. 14.

Table 2. 14. Profile shape parameters used in the eddy diffusion profile equation (2.27); ϕ, φ and ψ were determined by calibration and provided the best visual fit between simulated and observed phytoplankton profiles.

Location	ϕ	φ	ψ
NOA	0.45	0.1	1.0
MWY	0.45	0.07	1.0
SWA	0.45	0.05	1.0

The STL depth (h_{STL}) varied with time according to the time-varying Wedderburn Number (W_N) and depth to the density interface (h_1); development of W_N and h_1 are described in Section One.

2.4.1.2 Boundary Conditions

At the water surface, a no-flux boundary condition was used. At the bottom, particle concentrations were defined by sub-surface concentrations from the next profile (Table 2. 15). Bottom concentrations were not used because fluorescence response often diverged from particle concentrations, which indicated the bottom particles comprised particles other than chlorophyll *a*. Observed concentrations were used because the model does not simulate sediment re-suspension and deposition dynamics; however, sediment re-suspension dynamics are hypothesized to be an important process in inoculating the water column with *A. subarctica* (Gibson et al., 2003; Gibson and Fitzsimons, 1990).

Table 2. 15. Depth intervals that were used to calculate an average concentration that defined bottom concentrations in the model.

Station	Particle boundary depth interval (m)
NOA	35-38
MWY	45-50
SWA	20-25

2.4.1.3 Convective Mixing

The model used a simple convective mixing algorithm that uniformly mixed the water column over the convective depths specified in Table 2. 12. Convective mixing was activated when solar radiation was zero (night time) and mixing was maintained until solar radiation was greater than zero (day light), at which point mixing was governed by eddy diffusion.

2.4.1.4 Upwelling and Horizontal Transport

Upwelling and horizontal advection were simulated using (2.19) and applied only at SWA. Upwelling brings bottom water to the surface and bottom waters are entrained into the surface waters; this process dilutes the surface water. A down-welling process at NOA was not simulated because down-welling advects surface water downward but is suppressed from mixing across the density interface (Stevens and Imberger, 1996; Farrow and Stevens, 2003). Down-welling maintains a well-mixed surface layer but does not significantly dilute the surface water with bottom waters.

Upwelling was determined by the sign and value of the Wedderburn Number; upwelling was applied for $0<W_N<1.8$. The 1.8 value was determined through calibration but upwelling can occur for $W_N>1$ for linearly stratified systems (Monismith, 1986) and perhaps for systems between linearly stratified and a discrete step function. In (2.20), α and β are calibration coefficients, but β must constrain vertical velocity in the upper water column; Farrow and Stevens (2003) found vertical velocities were greatest in the upper 30% of the water column. Modeling results suggested α=0.003 and β=0.3 provided the best results based on visual inspection.

2.4.1.5 Diatom Sinking

Sinking velocities for *A. subarctica* can range from 0.1 m/d to 1.11 m/d with a mean of 0.86 m/d. The sinking appears to be dependent on phosphate and/or silica

concentrations but the literature does not provide a quantitative relation on the effect (Appendix B); therefore a constant settling velocity was used. The model was initialized with a settling velocity of 0.86 m/d and was calibrated to 0.8 m/d.

2.4.1.6 Respiration and Zooplankton Grazing

As stated previously, the 5+16 μm particle concentrations are a surrogate measure of the diatom population, which are negatively buoyant particles that contain living matter; the silica structure remains after the diatom dies. Assuming the silica structure remains unchanged whether it is living or dead (at least over the time it takes to sink from the water column into the sediments), the LISST-100 measures both live and dead phytoplankton cells. The respiration term in (2.21) quantifies the loss of life, it does not describe the loss or decay of cellular material. Because both live and dead cells were simulated, including respiration means that particles or cells would disappear or dissolve into the water column; dead cells can only sink to the bottom. For these reasons, respiration was eliminated from (2.21). This configuration has a negligible effect on the net growth rate because the omission of respiration can be compensated for by decreasing the maximum growth rate (2.33).

$$g_{\max} = \frac{1}{m_F}\left(g_{net} + r\right) \tag{2.33}$$

Where m_F is the multiple factor.

In the model, phytoplankton can be lost through zooplankton grazing (2.25), which requires zooplankton densities and grazing rates. During the 2004 spring diatom bloom, *D. (L.) ashlandi* copepod was the dominant herbivorous zooplankton species (Figure 2. 7). Zooplankton observations at SWA and NOA were not available until JD 90, 22 days after the start of the simulation period; therefore, the MWY observations were used for SWA and NOA (Table 2. 16). An initial filter rate of 2 ml/org/day was used and is within the range of values observed for adult *D. (L.) ashlandi*, filtering rates ranged from 0.46 ml/org/day to 37 ml/org/day (Appendix B).

Initially, the zooplankton densities included the adult and copepodids, but under this condition the phytoplankton did not grow; however, realistic growth response was obtained when only adult zooplankton densities were applied. The grazing restriction

to adults is suggested in the literature. Infante and Edmondson (1985) suggest *D. (L.) ashlandi* does not start eating *A. subarctica* until it reaches a length of 504 μm. And Moore (1979) found C-IV to C-VI *D. (L.) ashlandi* gut contents contained algae with significant amounts of detritus even though algae were abundant. The adult densities and lower grazing rate produced better visual fits to the observed particle profiles.

Table 2. 16. Adult *D. (L.) ashlandi* densities sampled near MWY. Adults comprise males and females.

Julian Day	Adults (org/l)	Copepodids (org/l)	Total Zooplankton density (org/l)
62.5	0.22	24	24.2
90.5	3.7	4.7	8.4
106.5	6.7	1.5	8.2
118.5	14	12	26

2.4.1.7 Temperature

Phytoplankton growth was controlled by temperature (2.23) with temperature profiles obtained from the SCAMP.

2.4.1.8 Light and Maximum Growth Rate

Photosynthesis varied over time and depth and included photo-inhibition effects (2.22). Initially, the maximum growth rate was set to 0.56 1/day (Appendix B), but phytoplankton did not grow. Sufficient growth was obtained for a maximum growth rate of 1.38 1/day, which is smaller than other modeling studies: 2.2 1/day (Arhonditsis and Brett, 2005a), 5.0 1/day (Cerco et al., 2004), and 2.4 1/day (Walters, 1980). The smaller growth rate could result from the omission of respiration (§2.4.1.6). The light attenuation coefficient was constant in space but varied with time (Table 2. 6).

2.4.1.9 Nutrients

Nutrient limitation was governed by (2.24) with phosphate being the limiting nutrient (Table 2. 7). An initial phosphate half-saturation constant of 0.006 mg/l was selected, but it was increased to 0.012 mg/l for better model response and because *A. subarctica* has a greater phosphate requirement than the general diatom population (Kilham et al., 1996; Interlandi et al., 1999; Appendix B).

2.4.2 Model Results

The model was applied to NOA, MWY, and SWA and best results (visual inspection) were obtained for the parameter set in Table 2. 17. The model was calibrated primarily to match phytoplankton (LISST 5+16 μm particle) concentrations in the STL and then secondarily to match concentration profiles below the STL. The model reproduced the rise and fall of phytoplankton at NOA and MWY reasonably well but had difficulty simulating conditions at SWA (Figure 2. 20, Figure 2. 21, and Figure 2. 22). In this section, LISST 5+16 μm particle concentrations and phytoplankton concentrations are use interchangeably.

Table 2. 17. Parameter values that produced the best model fit to observed particle concentrations.

Parameter	NOA	MWY	SWA
ϕ	0.45	0.45	0.45
ψ	1.0	1.0	1.0
φ	0.1	0.07	0.05
K_N for PO_4 (mg/l)	0.012	0.012	0.012
F_Z (l/org/day)	0.001	0.001	0.001
g_{max} (1/day)	1.38	1.38	1.38
W_S (m/d)	0.8	0.8	0.8
α	NA	NA	0.0033
β	NA	NA	0.3

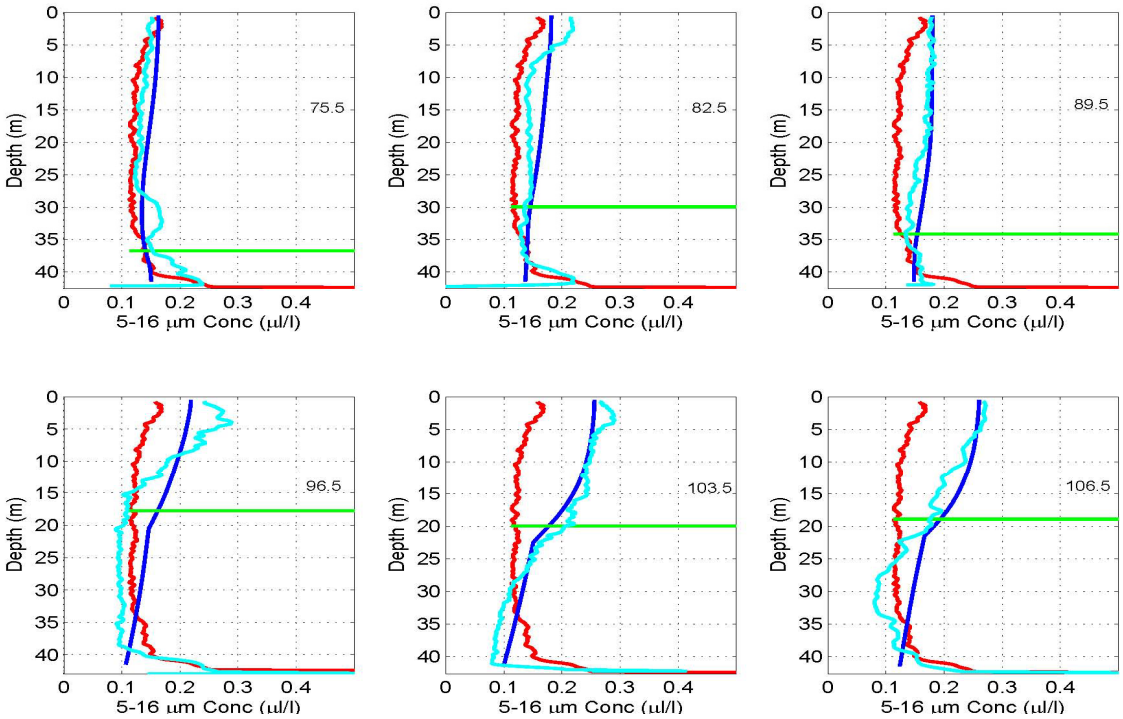

Figure 2. 20. NOA particle concentrations predicted by the model (blue) compared to observed concentrations (cyan), which combined 5 µm and 16 µm particles. Initial concentrations are represented by the red line, the green line is the STL depth, and sample day is on the right.

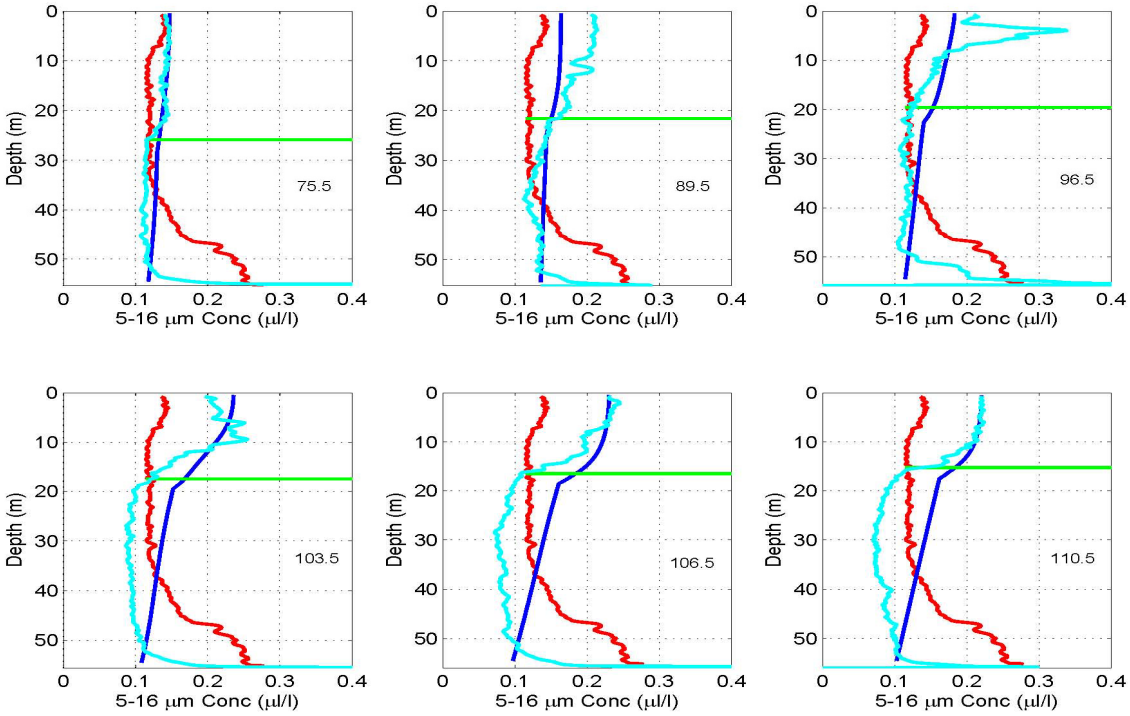

Figure 2. 21. MWY particle concentrations predicted by the model (blue) compared to observed concentrations (cyan), which combined 5 µm and 16 µm particles. Initial concentrations are represented by the red line, the green line is the STL depth, and sample day is on the right.